

ASPHERICAL PROPERTIES OF HYDRODYNAMICS AND NUCLEOSYNTHESIS IN JET-INDUCED SUPERNOVAE

NOZOMU TOMINAGA¹

Submitted to the Astrophysical Journal.

ABSTRACT

Jet-induced supernovae (SNe) have been suggested to occur in gamma-ray bursts (GRBs) and highly-energetic SNe (hypernovae). I investigate hydrodynamical and nucleosynthetic properties of the jet-induced explosion of a population III $40M_{\odot}$ star with a two-dimensional special relativistic hydrodynamical code. The abundance distribution after the explosion and the angular dependence of the yield are obtained for the models with high and low energy deposition rates $\dot{E}_{\text{dep}} = 120 \times 10^{51} \text{ergs s}^{-1}$ and $1.5 \times 10^{51} \text{ergs s}^{-1}$. I also find that the peculiar abundance pattern of a Si-deficient metal-poor star HE 1424-0241 can be reproduced by the angle-delimited yield for $\theta = 30^{\circ} - 35^{\circ}$ of the model with the energy deposition rate of $\dot{E}_{\text{dep}} = 120 \times 10^{51} \text{ergs s}^{-1}$. The ejection of Fe-peak products and the fallback of unprocessed materials can account for the abundance patterns of the extremely metal-poor (EMP) stars. I compare the yield of the jet-induced explosion with that of the spherical explosion and confirm the ejection and fallback in the jet-induced explosion model is almost equivalent to the “mixing-fallback” in spherical explosions. In contrast to the spherical models, however, the high-entropy environment realized in the jet-induced explosion enhances $[(\text{Sc}, \text{Ti}, \text{V}, \text{Cr}, \text{Co}, \text{Zn})/\text{Fe}]$. The enhancements of $[\text{Sc}/\text{Fe}]$ and $[\text{Ti}/\text{Fe}]$ improve agreements with the abundance pattern of the EMP stars.

Subject headings: Galaxy: halo — gamma rays: bursts — nuclear reactions, nucleosynthesis, abundances — stars: abundances — stars: Population II — supernovae: general

1. INTRODUCTION

Gamma-ray bursts (GRBs) are phenomena emitting γ -ray for short periods followed by a power-law decaying afterglow. The origin had been covered for a long while, but it has become clear that long GRBs are associated with supernovae (SNe). Three GRB-associated SNe have been observed so far: GRB 980425/SN 1998bw (Galama et al. 1998), GRB 030329/SN 2003dh (Stanek et al. 2003; Hjorth et al. 2003), and GRB 031203/SN 2003lw (Malesani et al. 2004). They are all energetic explosions of massive stars, called hypernovae (e.g., Nomoto et al. 2006, 2007 for a review).

Although the explosion mechanism of GRBs and GRB-associated SNe is still uncovered, the following photometric and spectroscopic observations indicate that they are aspherical explosions with jet(s). (1) The light curve of the GRB afterglow has shown a polychromatic break in the power-law decay. The break is called a “jet break” explained by the deceleration of the relativistic jet and the relativistic beaming of light (e.g., Frail et al. 2001; Piran 2005). (2) The nebular spectra of SN 1998bw show narrower $[\text{O I}]$ lines than $[\text{Fe II}]$ lines (Patat et al. 2001) indicating that O locates in the inner and lower-velocity region than Fe. This is realized in an aspherical explosion but not in a spherical explosion (Maeda et al. 2002, 2006).

The aspherical explosions are indirectly suggested from the abundance patterns of extremely metal-poor (EMP) stars with $[\text{Fe}/\text{H}] < -3$.² Such EMP stars

are likely to show the nucleosynthesis yields of a single or a few core-collapse SN/SNe (Audouze & Silk 1995; Beers & Christlieb 2005). The abundance patterns are reproduced by the “mixing-fallback” models that assume the extensive mixing of the shocked material before the fallback in a spherical SN model (Umeda & Nomoto 2002, 2003, 2005; Iwamoto et al. 2005; Tominaga et al. 2007b). Such a mixing is interpreted as a consequence of the aspherical explosion. Indeed, the abundance patterns of the EMP stars are reproduced by the jet-induced explosion model (Tominaga et al. 2007a).

Since the jet-induced SN contributes to many astrophysical phenomena, it is important to make a quantitative prediction on the nucleosynthesis outcome of the jet-induced explosions. In order to compare the jet-induced explosion models with the EMP stars, GRBs, and SNe, it is required to calculate multi-dimensional hydrodynamics and nucleosynthesis with the gravity and the relativity. Although there are many studies on the GRB jet using the special relativistic hydrodynamics (e.g., Aloy et al. 2000; Zhang et al. 2004; Mizuta et al. 2006), they did not include the gravity or calculate nucleosynthesis.

To investigate the yields of the jet-induced SNe, it is crucial to include the gravity because the fallback plays an important role on the nucleosynthesis yields. The studies by the use of Newtonian calculations have concluded that the energy deposition rate (\dot{E}_{dep}) sensitively affects SN nucleosynthesis (Maeda & Nomoto 2003; Nagataki et al. 2006). This result has been confirmed for the special relativistic cases (Tominaga et al. 2007a). In particular, Tominaga et al. (2007a) have shown that the jet-induced explosions with various \dot{E}_{dep}

¹ Department of Astronomy, School of Science, University of Tokyo, 7-3-1 Hongo, Bunkyo-ku, Tokyo, Japan; tominaga@astron.s.u-tokyo.ac.jp

² Here $[A/B] = \log_{10}(N_A/N_B) - \log_{10}(N_A/N_B)_{\odot}$, where the

subscript \odot refers to the solar value and N_A and N_B are the abundances of elements A and B, respectively.

can explain both the variations of the brightness of GRB-associated SNe and the variation of the abundance patterns of the EMP and hyper metal-poor (HMP, $[\text{Fe}/\text{H}] < -5$) stars.

The previous studies have proved mostly the angle-integrated yields and shown that the abundance patterns of the EMP stars are reproduced by the angle-integrated yield. However, the abundance distribution of the jet-induced explosion depends on the direction (e.g., Maeda & Nomoto 2003). Thus, the abundance patterns of the next-generation stars may well depend on the direction. I calculate aspherical stellar explosions induced by highly relativistic jets and obtain hydrodynamical and nucleosynthetic structures of such jet-induced explosion models. In particular, I investigate the angular dependence of the yield to compare the yields with the abundance patterns of the EMP and HMP stars.

In § 2, the applied models are described. In § 3, I present the hydrodynamical and nucleosynthetic structures of the jet-induced explosion model, investigate the angular dependence of the yields, and compared the jet-induced explosion model with the spherical SN model. In § 4, the conclusion and discussion are presented. In Appendixes, the hydrodynamics and nucleosynthesis code is described and tested.

2. MODELS

I investigate a jet-induced SN explosion of a Pop III $40M_{\odot}$ star (Umeda & Nomoto 2005; Tominaga et al. 2007b) by means of a two-dimensional relativistic Eulerian hydrodynamic and nucleosynthesis calculation with the gravity (Appendix A). The nucleosynthesis calculation is performed as a post-processing (Hix & Thielemann 1996, 1999) with the reaction network including 280 isotopes up to ^{79}Br (see Table 1 in Umeda & Nomoto 2005). The thermodynamic histories are traced by marker particles representing Lagrangian mass elements (e.g., Hachisu et al. 1990; Maeda & Nomoto 2003). A computational domain initially ranges up to the stellar surface where $R_{\text{star}} = 2 \times 10^7$ km and is captured by 200 logarithmical grids in the r -direction and 100 uniform grids in the θ -direction. A circumstellar matter (CSM) extends from the stellar surface with the slope $\rho \propto r^{-2}$.

The explosion mechanism of GRB-associated SNe is still under debate (e.g., a neutrino annihilation, Woosley 1993; MacFadyen & Woosley 1999; and a magnetorotation, Brown et al. 2000; Mizuno et al. 2004). Thus, I do not consider how the jet is launched, but I deal the jet parametrically with the following five parameters (Fig. B1): energy deposition rate (\dot{E}_{dep}), total deposited energy (E_{dep}), initial half angle of the jets (θ_{jet}), initial Lorentz factor (Γ_{jet}), and the ratio of thermal to total deposited energies (f_{th}). The jet is injected from the inner boundary at an enclosed mass M_0 corresponding to a radius R_0 . The jet is assumed to consist of the accreted matter and to expand adiabatically below the inner boundary. After the jet is injected to the computational domain, the thermodynamic histories are traced by the marker particles.

In this paper, I show three models; (A) a model with $\dot{E}_{\text{dep},51} = \dot{E}_{\text{dep}}/(10^{51}\text{ergs s}^{-1}) = 120$ and $M_0 = 1.4M_{\odot}$ ($R_0 = 900$ km), (B) a model with $\dot{E}_{\text{dep},51} = 1.5$

and $M_0 = 1.4M_{\odot}$ ($R_0 = 900$ km), and (C) a model with $\dot{E}_{\text{dep},51} = 120$ and $M_0 = 2.3M_{\odot}$ ($R_0 = 2700$ km). The other parameters are same for each model; $E_{\text{dep}} = 1.5 \times 10^{52}$ ergs, $\theta_{\text{jet}} = 15^\circ$, $\Gamma_{\text{jet}} = 100$ and $f_{\text{th}} = 10^{-3}$. The mass of jets is $M_{\text{jet}} \sim 8 \times 10^{-5}M_{\odot}$. The model parameters and the central remnant mass (M_{rem}) are summarized in Table B1. Models A and B are used in Tominaga et al. (2007a) and they reproduce the abundance patterns of the EMP stars³ (Cayrel et al. 2004) and HE 1327–2326 (e.g., Frebel et al. 2005, 2006; Collet et al. 2006), respectively.

3. RESULTS

The hydrodynamical calculations are followed until the homologously expanding structure is reached ($v \propto r$). Then, the ejected mass elements are identified from whether their radial velocities exceed the escape velocities at their position. The density structures of models A and B at $t = 10^5$ s are shown in Figure B2. The density along the jet axis is higher than the density along the equatorial plane and the SN ejecta of model A is denser and more compact than that of model B.

3.1. Fallback

Figures B3a and B3b show “accreted” regions for models A and B, where the accreted mass elements initially located in the progenitor. The O layer is separated into the two layers: (1) the O+Mg layer with $X(^{24}\text{Mg}) > 0.01$ and (2) the O+C layer with $X(^{12}\text{C}) > 0.1$. The inner matter is ejected along the jet-axis but not along the equatorial plane. On the other hand, the outer matter is ejected even along the equatorial plane, since the lateral expansion of the shock terminates the infall as the shock reaches the equatorial plane.

The accreted mass is larger for lower \dot{E}_{dep} . This stems from the balance between the ram pressures of the injecting jet (P_{jet}) and the infalling matter (P_{fall}) (e.g., Fryer 1999; Fryer & Mészáros 2003; Maeda & Tominaga 2007). The critical energy deposition rate ($\dot{E}_{\text{dep,cri}}$) giving $P_{\text{jet}} = P_{\text{fall}}$ is lower for the outer layer. Thus, the jet injection with lower \dot{E}_{dep} is realized at a later time when the central remnant becomes more massive. Additionally, the lateral expansion of the jet is more efficiently suppressed for lower \dot{E}_{dep} . As a result, the accreted region is larger and M_{rem} is larger for lower \dot{E}_{dep} .

A model with lower \dot{E}_{dep} has larger M_{rem} , higher $[\text{C}/\text{O}]$, $[\text{C}/\text{Mg}]$, and $[\text{C}/\text{Fe}]$, and smaller $M(\text{Fe})$ because of the larger amount of fallback (Tominaga et al. 2007a). The larger amount of fallback decreases the mass of the inner core (e.g., Fe, Mg, and O) relative to the mass of the outer layer (e.g., C, Figs. B3ab). Since O and Mg are synthesized in the inner layers than C, $[\text{C}/\text{O}]$ and $[\text{C}/\text{Mg}]$ are larger for the larger infall of the O layer. Also, the fallback of the O layer decreases $M(\text{Fe})$ because Fe is mainly synthesized explosively in the Si and O+Mg layers. Therefore, the variation of \dot{E}_{dep} in the jet-induced SN explosions predicts that the variations of $[\text{C}/\text{O}]$, $[\text{C}/\text{Mg}]$, and $[\text{C}/\text{Fe}]$ corresponding to the variation of $M(\text{Fe})$.

³ An averaged abundance pattern of four EMP stars, CS 22189–009, CS 22172–002, CS 22885–096, and CD –38 245, is adopted.

3.2. Abundance distribution

Figures B4a and B4b show the abundance distributions and density structures at $t = 10^5$ s for models A and B. I classify the mass elements by their abundances as follows: (1) Fe with $X(^{56}\text{Ni}) > 0.04$, (2) Si with $X(^{28}\text{Si}) > 0.08$, (3) O+Mg with $X(^{16}\text{O}) > 0.6$ and $X(^{24}\text{Mg}) > 0.01$, (4) O+C with $X(^{16}\text{O}) > 0.6$ and $X(^{12}\text{C}) > 0.1$, (5) He with $X(^4\text{He}) > 0.7$, and (6) H with $X(^1\text{H}) > 0.3$. If a mass element satisfies two or more conditions, the mass element is classified into the class with the smallest number.

The abundance distribution and thus the composition of the ejecta depend on the direction. In model A, the O+Mg, O+C, He, and H mass elements locate in the all direction. On the other hand, most of the Fe and Si mass elements locate at $\theta < 10^\circ$ and stratify in this order from the jet axis and a part of them locate at $15^\circ < \theta < 35^\circ$. Interestingly, the Fe mass elements surround the Si mass elements at $15^\circ < \theta < 35^\circ$. In model B, most of the O+C and He mass elements locate at $\theta < 3^\circ$, while the Fe mass elements injected as a jet expand laterally up to $\theta \sim 50^\circ$ and the H mass elements are distributed in the all directions. The lateral displacements of the Fe mass elements in models A and B are led by the collision with the stellar mantle and the internal pressure of the jet.

3.2.1. Angular dependence of the yields

I investigate the angle-delimited yields integrated over each 10° for models A and B, although the integration range might be too wide to be taken in a single next-generation star. Fe is mainly distributed within $\theta < 40^\circ$ for model A (Fig. B4a) and $\theta < 50^\circ$ for model B (Fig. B4b). Figures B5a and B5b show the abundance patterns of the angular-delimited yields for $\theta < 40^\circ$ of model A and $\theta < 50^\circ$ of model B, respectively. The yields are compared with the abundance patterns of the EMP stars (Cayrel et al. 2004) and the HMP stars (HE 0107–5240, e.g., Christlieb et al. 2002; Bessell & Christlieb 2005; Collet et al. 2006 and HE 1327–2326, e.g., Frebel et al. 2005, 2006; Collet et al. 2006).

Figure B5a shows the angle-delimited yields of model A. The abundance patterns of the angle-delimited yields are determined by which mass elements are included into the integration. Because of the stratified abundance distribution, the yields for $0^\circ \leq \theta < 10^\circ$ and $10^\circ \leq \theta < 20^\circ$ show low [C/Fe] and [O/Fe] and high [C/Fe] and [O/Fe], respectively. Intriguingly, the region with $30^\circ \leq \theta < 40^\circ$ includes the Fe mass elements in the outer layer and the O+Mg and O+C mass elements in the inner layer but not the Si mass elements. Thus, the yield for $30^\circ \leq \theta < 40^\circ$ shows a Si-deficient abundance pattern. Furthermore, the Fe and Si mass elements at $15^\circ < \theta < 35^\circ$ initially located along the jet axis ($\theta < 10^\circ$), and thus the high-entropy environment is realized in these mass elements and [Sc/Fe], [Ti/Fe], [Co/Fe], and [Zn/Fe] are enhanced in the yields for $10^\circ \leq \theta < 40^\circ$.

Figure B5b shows the angle-delimited yields of model B. The all angle-delimited yields of model B show high [C/Fe] as the angle-integrated yield. Since most of the heavy elements locate at $\theta < 10^\circ$, the yield for $\theta < 10^\circ$ is similar to the angle-integrated yield, except for N that is mostly contained in the H mass elements. On the other

hand, the yields for $10^\circ \leq \theta < 50^\circ$ consist of the Fe mass elements injected as a jet and the O+C mass elements. The differences of [C/Fe] and [Mg/Fe] in the yields for $10^\circ \leq \theta < 50^\circ$ mainly stem from the different amount of Fe ejection.

3.2.2. Abundance patterns of the metal-poor stars

A very peculiar, Si-deficient, metal-poor star HE 1424–0241 was observed (Cohen et al. 2006). Its abundance pattern with high [Mg/Si] (~ 1.4) and normal [Mg/Fe] (~ 0.4) is difficult to be reproduced by previous SN models. This is because $\log\{[X(^{24}\text{Mg})/X(^{28}\text{Si})]/[X(^{24}\text{Mg})/X(^{28}\text{Si})]_\odot\} \lesssim 1.6$ is realized in the O+Mg layer at the presupernova stage (e.g., Woosley & Weaver 1995; Umeda & Nomoto 2005). Thus, in order to reproduce the abundance pattern of HE 1424–0241, the SN yield is required to consist of explosively-synthesized Fe but not explosively-synthesized Si.

The angle-delimited yield may possibly explain the high [Mg/Si] and normal [Mg/Fe] (Fig. B5c). Figure B5c shows that the yield integrated over $30^\circ - 40^\circ$ or $30^\circ - 35^\circ$ of model A reproduces the abundance pattern of HE 1424–0241. The yield consist of Mg in the inner region and Fe in the outer region (Fig. B4a). Although there are some elements to be improved, the elusive feature of HE 1424–0241 could be explained by taking into account the angular dependence of the yield. The high [Mg/Si] and normal [Mg/Fe] can be realized with an appropriate integration range if the Fe mass elements penetrate the stellar mantle (i.e., the duration of the jet injection is long) and if the O+Mg mass elements are ejected in all directions (i.e., \dot{E}_{dep} is high).

If the yield depends on the direction, the abundance patterns of the angle-delimited yields have a large scatter (Fig. B5a). On contrary, the observations of the EMP stars provide abundance ratios with comparatively small scatters (e.g., Cayrel et al. 2004). This implies the following: the abundance patterns of the normal EMP stars require strong mixing of the SN ejecta, e.g., due to the interaction with interstellar medium (ISM), so that the yield no longer depends on the direction, while the abundance pattern of HE 1424–0241 requires weak mixing of the SN ejecta. Actually, it was suggested that the interaction between the SN ejecta and ISM could induce further mixing of the abundances if ISM has inhomogeneous structure (e.g., Nakasato & Shigeyama 2000). Thus, in order to conclude the origin of HE 1424–0241, it is necessary to calculate three-dimensional evolution of a supernova remnant in the inhomogeneous ISM.

3.3. Comparison with the spherical supernova model

The calculations of the jet-induced explosions show that the ejection of the inner matter is compatible with the fallback of the outer matter (Figs. B3ab). This is consistent with the two-dimensional illustration of the mixing-fallback model (Fig. 12b in Tominaga et al. 2007b).

In this subsection, I clarify the relation between the mixing-fallback model and the jet-induced explosion model. The mixing-fallback model has three parameters; initial mass cut [$M_{\text{cut}}(\text{ini})$], outer boundary of the mixing region [$M_{\text{mix}}(\text{out})$], and a fraction of matter ejected from

the mixing region (f). The remnant mass is written as

$$M_{\text{rem}} = M_{\text{cut}}(\text{ini}) + (1 - f)[M_{\text{mix}}(\text{out}) - M_{\text{cut}}(\text{ini})]. \quad (1)$$

The three parameters would relate to the hydrodynamical properties of the jet-induced explosion models, e.g., the inner boundary (M_0), the outer edge of the accreted region ($M_{\text{acc,out}}$), and the width between the edge of the accreted region and the jet axis.

I apply model C to compare the yield of the jet-induced SN explosion with the yield of the spherical SN explosion applied the mixing-fallback model. The inner boundary, the outer edge of the accreted region, and the central remnant mass of model C are $M_0 = 2.3M_\odot$, $M_{\text{acc,out}} = 12.2M_\odot$, and $M_{\text{rem}} = 8.1M_\odot$. The abundance distribution of model C at $t = 10^5$ s is shown in Figure B6a.

Figure B6b shows the initial positions of the ejected mass elements in model C. Color of the marks represents the composition of the mass elements. Explosive nucleosynthesis takes place in the mass elements between the edge of the accreted region and the jet axis. Thus, the amounts of the explosive nucleosynthesis products may well be reduced relative to the spherical explosions. The shock collision at the equatorial plane realizes the matter ejection of the deep O+Mg layer along the equatorial plane. Although the mass ejection could be due to the reflective boundary condition on the equatorial plane, this does not affect the following discussion because the amount of the matter ejection is small.

I compare the angle-integrated yield of model C with the yields of the spherical SN model with $M_{\text{ms}} = 40M_\odot$ and $E_{51} = 30$ applied the mixing-fallback model (Fig. B6c). Here, I set $M_{\text{cut}}(\text{ini})$ to be same as M_0 [i.e., $M_{\text{cut}}(\text{ini}) = 2.3M_\odot$] and apply three sets of parameters, $M_{\text{mix}}(\text{out})$ and f , as follows:

(1) $M_{\text{mix}}(\text{out}) = 12.2M_\odot$ and $f = 0.41$. $M_{\text{mix}}(\text{out})$ corresponds to $M_{\text{acc,out}}$ and f is the ratio of the ejected mass and the total mass between M_0 and $M_{\text{acc,out}}$.

(2) $M_{\text{mix}}(\text{out}) = 10.3M_\odot$ and $f = 0.27$. f is the fraction of the solid angle of the region where the ejected mass elements located at $r \sim 10^3$ km (the Si-burning region, hereafter the fraction is written as f_{Si}). $M_{\text{mix}}(\text{out})$ is set to yield the same M_{rem} as model C.

(3) $M_{\text{mix}}(\text{out}) = 10.8M_\odot$ and $f = 0.19$. f and $M_{\text{mix}}(\text{out})$ are set to yield the most resemblant abundance pattern to model C. As a result, $M_{\text{rem}} (= 9.2M_\odot)$ is slightly larger than M_{rem} of model C.

Figure B6c shows that the angle-integrated abundance pattern of model C is roughly reproduced by the mixing-fallback model with the parameter sets of (2) and (3). Thus, I conclude that the jet-induced explosion is mimicked by the mixing-fallback model reasonably. M_0 , f_{Si} , and M_{rem} in the jet-induced explosion model are represented by $M_{\text{cut}}(\text{ini})$, f , and M_{rem} in the mixing-fallback model, respectively.

There are some elements showing differences, Sc, Ti, V, Cr, Co, and Zn. The enhancements of [Sc/Fe] and [Ti/Fe] improve agreements with the observations. The differences stem from the high-entropy explosion due to the concentration of the energy injection (e.g., Maeda & Nomoto 2003). In particular, Sc is the most sensitive element to the entropy and [Sc/Fe] is more enhanced for the deeper M_0 because of the weaker lateral expansion (Fig. B5a). Such thermodynamical

feature of the jet-induced explosion model cannot be mimicked by the mixing-fallback model exactly, although a “low-density” modification might mimic the high-entropy environment (e.g., Umeda & Nomoto 2005; Tominaga et al. 2007b).

4. CONCLUSIONS AND DISCUSSION

I perform two-dimensional hydrodynamical and nucleosynthesis calculations of the jet-induced explosions of a Pop III $40M_\odot$ star. Here I test three jet-induced explosion models A, B, and C as summarized in Table B1 and conclude as follows.

(1) **Fallback:** the dynamics and the abundance distributions depend sensitively on the energy deposition rate \dot{E}_{dep} . The explosion with lower \dot{E}_{dep} leads to a larger amount of fallback, and consequently smaller $M(\text{Fe})$ and higher [C/O], [C/Mg], and [C/Fe]. Such dependences of [C/Fe] and $M(\text{Fe})$ on \dot{E}_{dep} predict that the higher [C/Fe] tends to be realized for lower [Fe/H]. Note, however, the formation of star with low [C/Fe] and [Fe/H] is possible because [Fe/H] depends on the swept-up H mass, i.e., the interaction between the SN ejecta and ISM (e.g., Cioffi et al. 1988).

(2) **Angular dependence:** I present the aspherical abundance distributions and investigate the angular dependence of the yield. Although the angle-delimited yields of model A have a large scatter that may be inconsistent with the small scatter in the abundance ratios of the normal EMP stars, the angle-delimited yield could reproduce the extremely peculiar abundance pattern of HE 1424-0241. On the other hand, the angle-delimited yields of model B shows high [C/Fe] as the angle-integrated yield.

The angle-delimited yield depends strongly on which mass elements are included into the integration. This would be determined by the abundance mixing in the SN ejecta and by the region where the next-generation star takes in the metal-enriched gas. Although it is necessary to calculate three-dimensional evolution of the supernova remnant, these would be interesting issues.

(3) **Comparison with the spherical explosion:** the angle-integrated yield of the jet-induced explosion is well reproduced by a spherical SN model applied the mixing-fallback model. This confirms that the mixing-fallback model mimics the jet-induced explosion well. This is because the abundance ratios between elements synthesized in different regions (e.g., C, O, Mg, and Fe) depend on the hydrodynamical structure of the explosion. Such macroscopic properties of the jet-induced SN are represented by the mixing-fallback model.

On the other hand, the ratios between the explosively-synthesized elements depend on the thermodynamical properties of the explosion. In particular, [Sc/Fe], [Ti/Fe], [V/Fe], [Cr/Fe], [Co/Fe] and [Zn/Fe] are enhanced by the high-entropy environment in the jet-induced explosion, thus showing differences from the mixing-fallback model. The enhancement of [Sc/Fe] and [Ti/Fe] improve the agreement with the observations. Note, the enhancement of [Ti/Fe] relative to the spherical SN model in this paper is larger than in Maeda & Nomoto (2003). This might be because the relativistic jet suppresses the lateral expansion and enhances the energy concentration.

This work formed a part of the author's PhD thesis (Tominaga 2007, completed in September 2007). The author would like to thank H. Umeda, K. Maeda, K. Nomoto, N. Iwamoto for providing the progenitor

models and valuable discussion. The author is supported through the JSPS (Japan Society for the Promotion of Science) Research Fellowship for Young Scientists.

APPENDIX

SPECIAL RELATIVISTIC HYDRODYNAMIC CODE

I develop a two-dimensional special relativistic Eulerian hydrodynamic code with Marquina's flux formula (Donat et al. 1998) and with a conversion method from the observer frame to the proper frame (Martí & Müller 1996). This code applies third order Runge-Kutta method in time of Shu & Osher (1988, see also Aloy et al. 1999) and second order piecewise hyperbolic method (PHM) in space of Marquina (1994).

The equations of special relativistic hydrodynamics are described in terms of a four-velocity vector field and an energy momentum tensor (Martí & Müller 1994). Physical quantities in a rest frame (relativistic rest-mass density: D , the i -th components of momentum densities: S_i , and energy density: τ) and a comoving frame are related as follows:

$$\begin{aligned} D &= \rho \Gamma \\ S_i &= \rho h \Gamma^2 v_i \\ \tau &= \rho h \Gamma^2 - p - \rho \Gamma \end{aligned}$$

where the light velocity is set to $c = 1$, ρ is the proper rest-mass density, v_i are the i -th components of velocities, $\Gamma = 1/\sqrt{1 - \sum_i v_i^2}$ is the Lorentz factor of the fluid element with respect to the rest frame, p is the proper pressure, and $h = 1 + e/\rho + p/\rho$ is the specific enthalpy (here, e is the proper internal energy per unit volume).

The basic equations in the special relativistic hydrodynamics are written in spherical polar coordinates (r, θ) as

$$\frac{\partial D}{\partial t} + \frac{\partial(r^2 D v_r)}{\partial(r^3/3)} + \frac{1}{r} \frac{\partial(\sin \theta D v_\theta)}{\partial(-\cos \theta)} = 0 \quad (\text{A1})$$

$$\frac{\partial S_r}{\partial t} + \frac{\partial(S_r v_r + p)}{\partial r} + \frac{1}{r} \frac{\partial(\sin \theta S_r v_\theta)}{\partial(-\cos \theta)} = -2 \frac{S_r v_r}{r} + \frac{S_\theta v_\theta}{r} + g_r \rho \quad (\text{A2})$$

$$\frac{\partial S_\theta}{\partial t} + \frac{\partial(r^2 S_\theta v_r)}{\partial(r^3/3)} + \frac{1}{r} \frac{\partial(S_\theta v_\theta + p)}{\partial \theta} = -\frac{1}{r} \frac{\cos \theta}{\sin \theta} - \frac{S_\theta v_r}{r} + g_\theta \rho \quad (\text{A3})$$

$$\frac{\partial \tau}{\partial t} + \frac{\partial\{r^2(S_r - D v_r)\}}{\partial(r^3/3)} + \frac{1}{r} \frac{\partial\{\sin \theta(S_\theta - D v_\theta)\}}{\partial(-\cos \theta)} = (g_r v_r + g_\theta v_\theta) \rho \quad (\text{A4})$$

where g_i ($i = r, \theta$) are the i -th gravitational acceleration components. The gravitational potential includes the contributions of the self-gravity and the central remnant (Hachisu 1986). The equations are an equation of continuity, momentum conservation equations, an energy conservation equation.

One-dimensional Riemann problems

The code is tested with the one-dimensional shock tube problems (e.g., Martí & Müller 1994). I set the computational region $0 \leq x \leq 1$ where $c = 1$ that is divided into two regions, i.e., left and right regions, at $x = 0.5$. The density (ρ), pressure (p), and velocity (v) of left and right regions are represented by L and R subscripts, respectively. The time variation is derived by the analytical solution of the Riemann problem (Martí & Müller 1994). I test three problems with 10^3 uniform meshes ($\Delta x = 1/10^3$) and a constant adiabatic index. The initial states are as follows:

Problem (a) $\gamma = 5/3$

$$\begin{aligned} (\rho_L, p_L, v_L) &= (1, 10^3, 0) \text{ at } 0.0 \leq x \leq 0.5 \\ (\rho_R, p_R, v_R) &= (1, 0.01, 0) \text{ at } 0.5 \leq x \leq 1.0 \end{aligned}$$

Problem (b) $\gamma = 4/3$

$$\begin{aligned} (\rho_L, p_L, \Gamma_L) &= (1, 1, 10^3) \text{ at } 0.0 \leq x \leq 0.5 \\ (\rho_R, p_R, \Gamma_R) &= (1, 10^6, 1) \text{ at } 0.5 \leq x \leq 1.0 \end{aligned}$$

Problem (c) $\gamma = 4/3$

$$\begin{aligned} (\rho_L, p_L, v_L) &= (1, 10, -0.9) \text{ at } 0.0 \leq x \leq 0.5 \\ (\rho_R, p_R, v_R) &= (10, 100, 0.9) \text{ at } 0.5 \leq x \leq 1.0 \end{aligned}$$

The analytical solutions are reproduced by the calculations (Figs. B7abc). The agreements confirm that the code correctly solves left- and right-oriented rarefaction and shock waves.

Two-dimensional shock tube problem

The two-dimensional shock tube problem was proposed by Del Zanna & Bucciantini (2002) and repeated by subsequent studies (e.g., Lucas-Serrano et al. 2004; Zhang & MacFadyen 2006; Mizuta et al. 2006). I test the problem with $10^3 \times 10^3$ square uniform meshes. In this problem, the two-dimensional region ($0 \leq x \leq 1, 0 \leq y \leq 1$) are divided into the following four regions:

$$\begin{aligned} (\rho, p, v_x, v_y) &= (0.50, 1.00, 0.00, 0.00) \text{ at } 0.0 \leq x \leq 0.5, 0.0 \leq y \leq 0.5 \\ (\rho, p, v_x, v_y) &= (0.10, 1.00, 0.99, 0.00) \text{ at } 0.0 \leq x \leq 0.5, 0.5 \leq y \leq 1.0 \\ (\rho, p, v_x, v_y) &= (0.10, 0.01, 0.00, 0.00) \text{ at } 0.5 \leq x \leq 1.0, 0.0 \leq y \leq 0.5 \\ (\rho, p, v_x, v_y) &= (0.10, 1.00, 0.00, 0.99) \text{ at } 0.5 \leq x \leq 1.0, 0.5 \leq y \leq 1.0 \end{aligned}$$

where v_i ($i = x, y$) are the i -th components of velocities and the adiabatic index is $\gamma = 5/3$. Figure B8 shows color contours of $\log(\rho)$ at $t = 0.4$.

Double Mach reflection problem

Woodward & Colella (1984) introduced the double Mach reflection problem of a strong shock in the Newtonian case and the problem was extended to the special relativistic case (Zhang & MacFadyen 2006; Mizuta et al. 2006). I test the code with the same initial conditions as in the previous studies (Zhang & MacFadyen 2006; Mizuta et al. 2006). The computational region is a $0 \leq x \leq 4, 0 \leq y \leq 1$ rectangle captured by 512×128 uniform square meshes. The density and pressure of the unshocked gas, the adiabatic index, and the classical Mach number ($M_c \equiv V_S/c_s$, where V_S is a shock velocity and c_s is a sound speed) are set to be $\rho = 1.4$, $p = 0.0025$, $\gamma = 1.4$, and $M_c = 10$ respectively. Thus, the shock velocity is $V_S = 0.4984$ and the density, pressure, and velocity of the post-shock gas are $\rho = 8.564$, $p = 0.3804$, and $v = 0.4247$. The shock front is initially set to cross the x axis at $x = 1/6$ with an angle of 60° . The initial conditions are as follows:

$$\begin{aligned} (\rho, p, v_x, v_y) &= (1.4, 0.0025, 0.00, 0.00) \text{ at } x - y \tan 60^\circ < 1/6 \\ (\rho, p, v_x, v_y) &= (8.564, 0.3804, 0.4247 \sin 60^\circ, 0.4247 \cos 60^\circ) \text{ at } x - y \tan 60^\circ > 1/6. \end{aligned}$$

The boundary conditions are inflow of the post-shock gas at $x = 0$, at $0 \leq x \leq 1/6$ in $y = 0$ axis, and at $0 \leq x \leq (1/6 + \tan 60^\circ + V_S t / \sin 60^\circ)$ in $y = 1$ axis, reflective boundaries at $1/6 < x < 4$ in $y = 0$ axis, and freely inflow and outflow conditions at the other boundaries. Figure B9 shows thirty-level iso-surfaces of $\log(\rho)$ at $t = 4.0$.

Emery step problem

The wind tunnel problem with a reflecting step, called the Emery step problem, was introduced by Emery (1968) and repeated by subsequent studies (Zhang & MacFadyen 2006; Mizuta et al. 2006). The computational domain is a $0 \leq x \leq 3, 0 \leq y \leq 1$ rectangle captured by 240×80 uniform square meshes. The domain is filled by a gas with $\rho = 1.4$, $p = 0.1534$, and $v = 0.999$. The pressure is set so that $M_c = 3$. The wind tunnel has the reflecting step locating at $0.6 \leq x$ and $y \leq 0.2$. The following boundary conditions are applied: the upper and lower boundaries are reflective and the boundaries at $x = 0$ and $x = 3$ are open. Figure B10 shows thirty-level iso-surfaces of $\log(\rho)$ at $t = 4.0$.

NUCLEOSYNTHESIS CALCULATION

The two-dimensional special relativistic hydrodynamical calculation does not include nuclear energy releases and applies a constant adiabatic index $\gamma = 4/3$. The proper internal energy is written as $e = p/(\gamma - 1)$. Temperature T is derived with an analytical equation of state including radiation and e^-e^+ pair (e.g., Freiburghaus et al. 1999) as follows:

$$e = aT^4 \left\{ 1 + \frac{7}{4} \cdot \frac{T_9^2}{T_9^2 + 5.3} \right\}. \quad (\text{B1})$$

where $a = 7.57 \times 10^{-15}$ ergs cm^{-3} K^{-4} is the radiation-density constant and $T_9 = T/10^9$ K.

I calculate explosive nucleosynthesis in a non-relativistic spherical explosion of a $40M_\odot$ star with 3×10^{52} ergs. The post-processing calculations are performed with the thermodynamic histories obtained by the two-dimensional special relativistic Eulerian hydrodynamics code and a one-dimensional Lagrangian hydrodynamics code used in Umeda & Nomoto (2002, 2005), and Tominaga et al. (2007b). The one-dimensional Lagrangian hydrodynamical calculation includes nuclear energy releases from α network and the equation of state includes the gas, radiation, e^-e^+ pair (Sugimoto & Nomoto 1975), Coulomb interactions between ions and electrons, and phase transition (Nomoto et al. 1982; Nomoto & Hashimoto 1988). The abundance distributions derived by both calculations are consistent (Figs. B11ab). This consistency justifies the results of the two-dimensional special relativistic hydrodynamics and nucleosynthesis calculations even with the simple assumptions.

TABLE B1
JET-INDUCED EXPLOSION MODELS.

Name	M_0 [M_\odot]	R_0 [km]	\dot{E}_{dep} [$10^{51} \text{ ergs s}^{-1}$]	E_{dep} [10^{51} ergs]	θ_{jet} [degrees]	Γ_{jet}	f_{th}	M_{rem} [M_\odot]
A	1.4	900	120	15	15	100	10^{-3}	9.1
B	1.4	900	1.5	15	15	100	10^{-3}	16.9
C	2.3	2700	120	15	15	100	10^{-3}	8.1

REFERENCES

- Aloy, M.A., Ibáñez, J.M^a, Martí, J.M^a, & Müller, E. 1999, ApJS, 122, 151
- Aloy, M.A., Müller, E., Ibáñez, J.M^a, Martí, J.M^a, & MacFadyen, A. 2000, ApJ, 531, L119
- Audouze, J., & Silk, J. 1995, ApJ, 451, L49
- Beers, T.C., & Christlieb, N. 2005, ARA&A, 43, 531
- Bessell, M. S., & Christlieb, N. 2005, in From Lithium to Uranium: Elemental Tracers of Early Cosmic Evolution. eds. Hill, V., et al., (Cambridge: Cambridge University Press), 228, 237
- Brown, G.E., Lee, C.-H., Wijers, R.A.M.J., Lee, H.K., Israelian, G., & Bethe, H.A. 2000, New Astronomy, 5, 191
- Cayrel, R., et al. 2004, A&A, 416, 1117
- Christlieb, N., et al. 2002, Nature, 419, 904
- Cioffi, D. F., McKee, C. F., Bertschinger, E. 1988, ApJ, 334, 252
- Cohen, J.G., et al. 2006, AJ, 132, 137
- Collet, R., Asplund, M., & Trampedach, R. 2006, ApJ, 644, L121
- Del Zanna, L., & Bucciantini, N. 2002, A&A, 390, 1177
- Donat, R., Font, J.A., Ibáñez, J.M^a, & Marquina, A. 1998, J. Comput. Phys., 146, 58
- Emery, A.F. 1968, J. Comp. Phys., 2, 306
- Frail, D.A., et al. 2001, ApJ, 562, L55
- Frebel, A., et al. 2005, Nature, 434, 871
- Frebel, A., Christlieb, N., Norris, J. E., Aoki, W., & Asplund, M. 2006, ApJ, 638, L17
- Freiburghaus, C., Rembges, J.-F., Rauscher, T., Kolbe, E., Thielemann, F.-K., Kratz, K.-L., Pfeiffer, B., & Cowan, J. J. 1999, ApJ, 516, 381
- Fryer, C. L. 1999, ApJ, 522, 413
- Fryer, C. L., & Mészáros, P. 2003, ApJ, 588, L25
- Galama, T. J., et al. 1998, Nature, 395, 670
- Hachisu, I. 1986, ApJS, 62, 461
- Hachisu, I., Matsuda, T., Nomoto, K., & Shigeyama, T. 1990, ApJ, 358, L57
- Hix, W. R., & Thielemann, F.-K. 1996, ApJ, 460, 869
- Hix, W. R., & Thielemann, F.-K. 1999, ApJ, 511, 862
- Hjorth, J., et al. 2003, Nature, 423, 847
- Iwamoto, N., Umeda, H., Tominaga, N., Nomoto, K., Maeda, K. 2005, Science, 309, 451
- Lucas-Serrano, A., Font, J.A., Ibáñez, J.M., & Martí, J.M. 2004, A&A, 428, 703
- MacFadyen, A. I., & Woosley, S. E. 1999, ApJ, 524, 262
- Maeda, K., Nakamura, T., Nomoto, K., Mazzali, P.A., Patat, F., & Hachisu, I. 2002, ApJ, 565, 405
- Maeda, K., & Nomoto, K., 2003, ApJ, 598, 1163
- Maeda, K., Mazzali, P. A., & Nomoto, K. 2006, ApJ, 645, 1331
- Maeda, K., & Tominaga, N. 2007, in preparation.
- Malesani, D., et al. 2004, ApJ, 609, L5
- Marquina, A. 1994, SIAM J. Sci. Comput., 15, 892
- Martí, J.M., & Müller, E. 1994, J. Fluid Mech., 258, 317
- Martí, J.M., & Müller, E. 1996, J. Comput. Phys., 123, 1
- Mizuno, Y., Yamada, S., Koide, S., & Shibata, K. 2004, ApJ, 615, 389
- Mizuta, A., Yamasaki, T., Nagataki, S., Mineshige, S. 2006, ApJ, 651, 960
- Nagataki, S., Mizuta, A., & Sato, K. 2006, ApJ, 647, 1255
- Nakamura, N., & Shigeyama, T. 2000, ApJ, 541, L59
- Nomoto, K. 1982, ApJ, 253, 798
- Nomoto, K., & Hashimoto, M. 1988, Phys. Rep., 163, 13
- Nomoto, K., Tominaga, N., Umeda, H., Kobayashi, C., & Maeda, K. 2006, Nucl. Phys. A, 777, 424 (astro-ph/0605725)
- Nomoto, K., et al. 2007, *Nuovo Cimento*, 121, 1207 (astro-ph/0702472)
- Patat, F., et al. 2001, ApJ, 555, 900
- Piran, T. 2005, Rev. Mod. Phys., 76, 1143
- Shu, C. W., & Osher, S. J. 1988, J. Comput. Phys., 105, 92
- Stanek, K. Z., et al. 2003, ApJ, 591, L17
- Sugimoto, D., & Nomoto, K. 1975, Sci. Pap. Coll. Gen. Educ. Univ. Tokyo, 25, 109
- Tominaga, N., Maeda, K., Umeda, H., Nomoto, K., Tanaka, M., Iwamoto, N., Suzuki, T. & Mazzali, P. 2007a, ApJ, 657, L77
- Tominaga, N., Umeda, H., & Nomoto, K. 2007b, ApJ, 660, 516
- Tominaga, N. 2007, PhD thesis, University of Tokyo
- Umeda, H., & Nomoto, K. 2002, ApJ, 565, 385
- Umeda, H., & Nomoto, K. 2003, Nature, 422, 871
- Umeda, H., & Nomoto, K. 2005, ApJ, 619, 427
- Woodward, P.R., & Colella, P. 1984, J. Comp. Phys., 54, 115
- Woosley, S.E., 1993, ApJ, 405, 273
- Woosley, S. E., & Weaver, T. A. 1995, ApJS, 101, 181
- Zhang, W., Woosley, S.E., & Heger, A., 2004, ApJ, 608, 365
- Zhang, W., & MacFadyen, A.I. 2006, ApJS, 164, 255

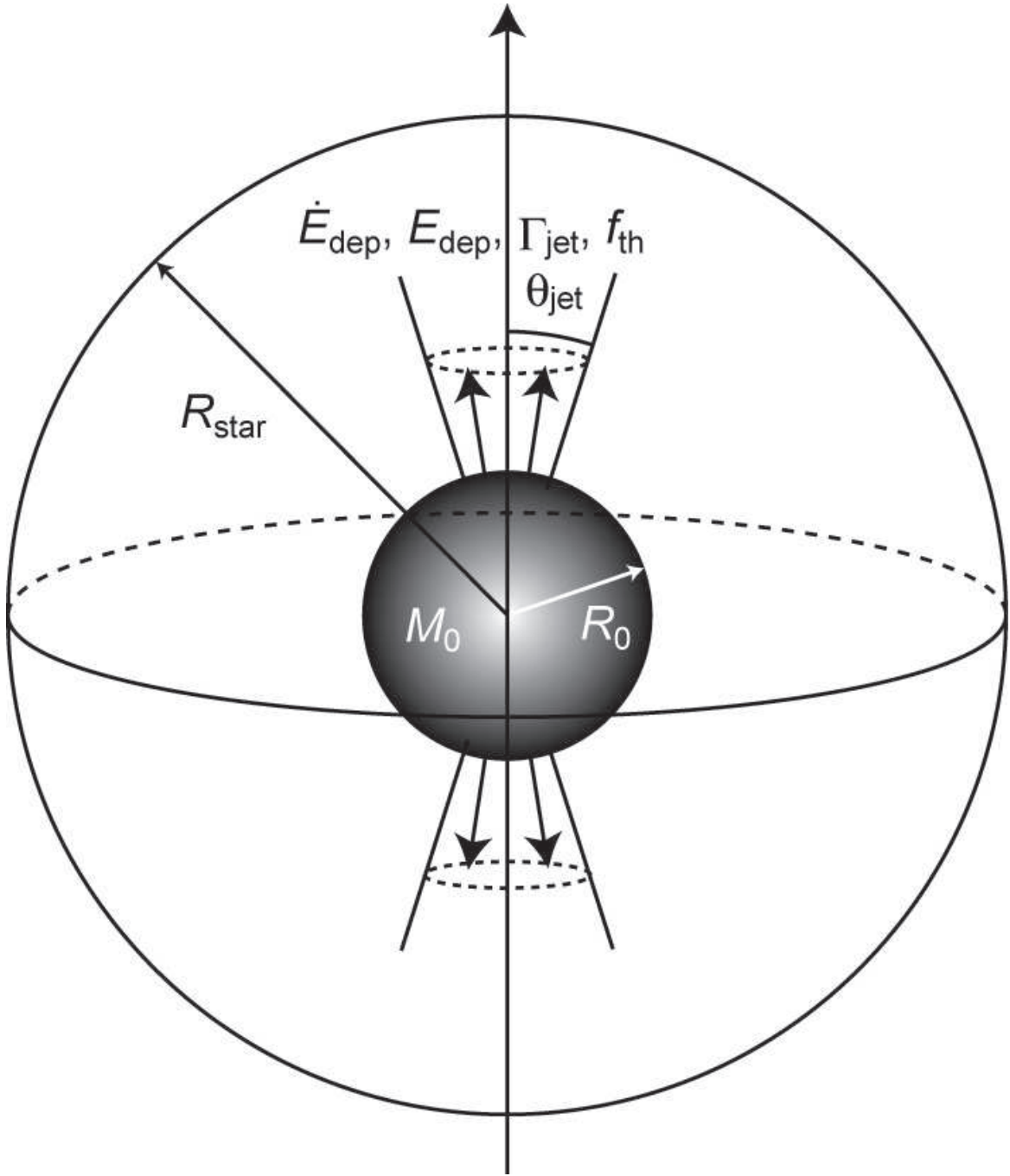


FIG. B1.— Schematic picture of the jet-induced explosion.

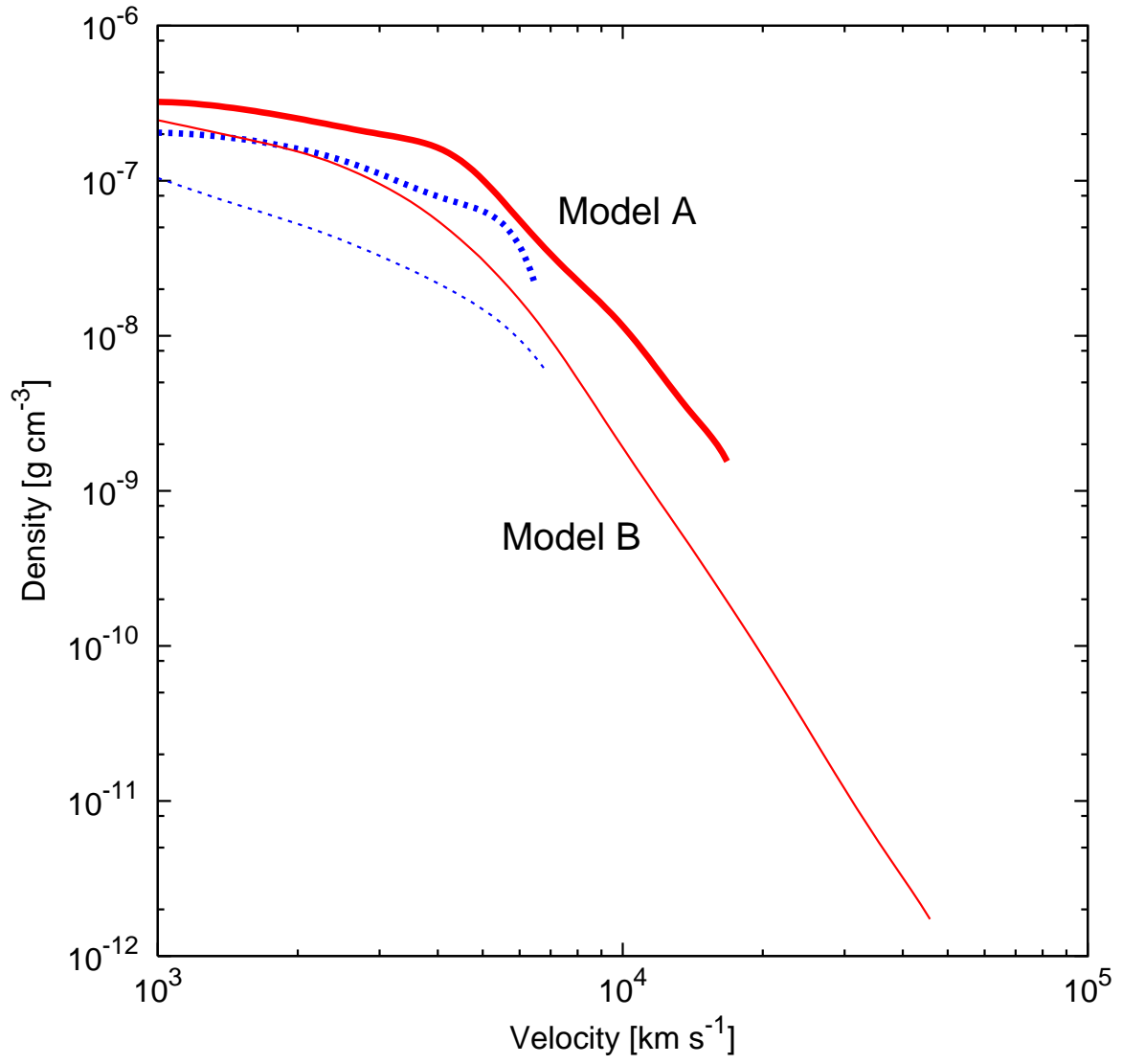


FIG. B2.— Density structures at $t = 10^5$ s along the jet axis (*solid*) and the equatorial plane (*dashed*) of model A (*thick*) and B (*thin*).

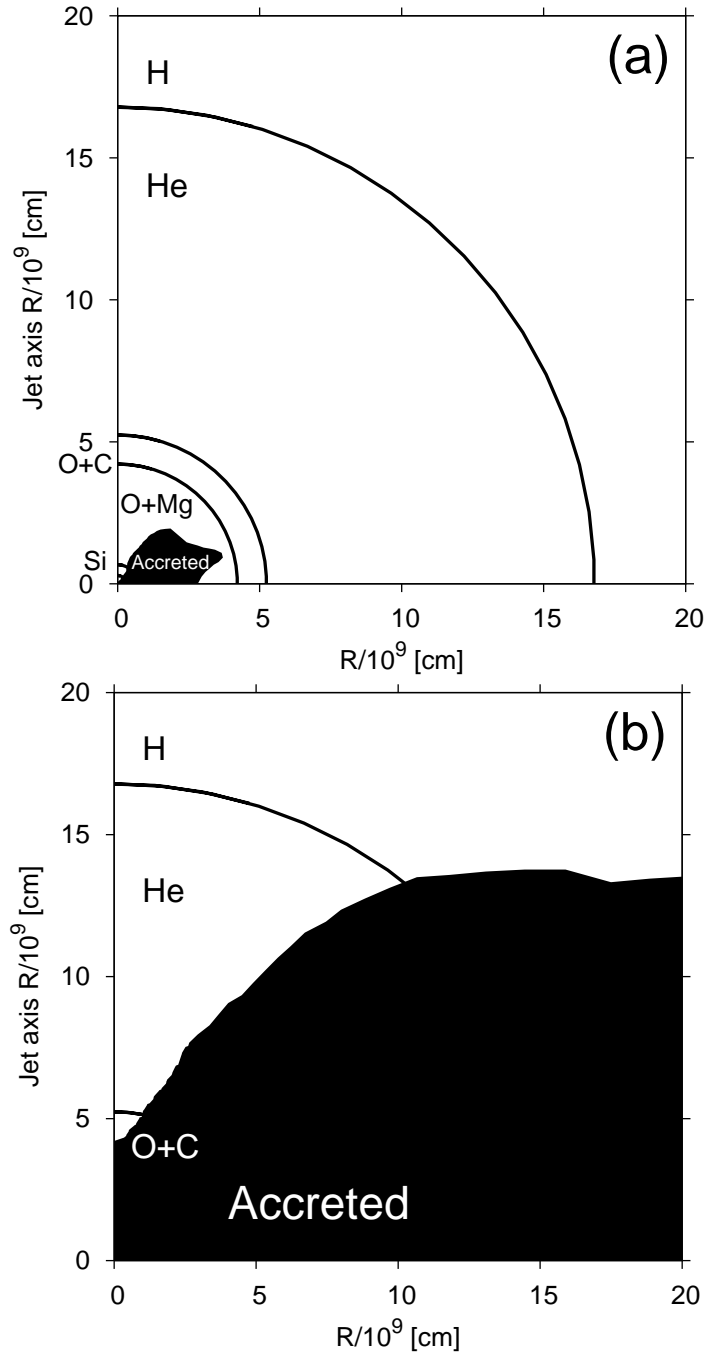


FIG. B3.— Initial locations of the mass elements which are finally accreted (*black*), for (a) model A and (b) model B. The background circles represent the layers in the progenitor star; the H, He, O+C, O+Mg, and Si layers from the outside.

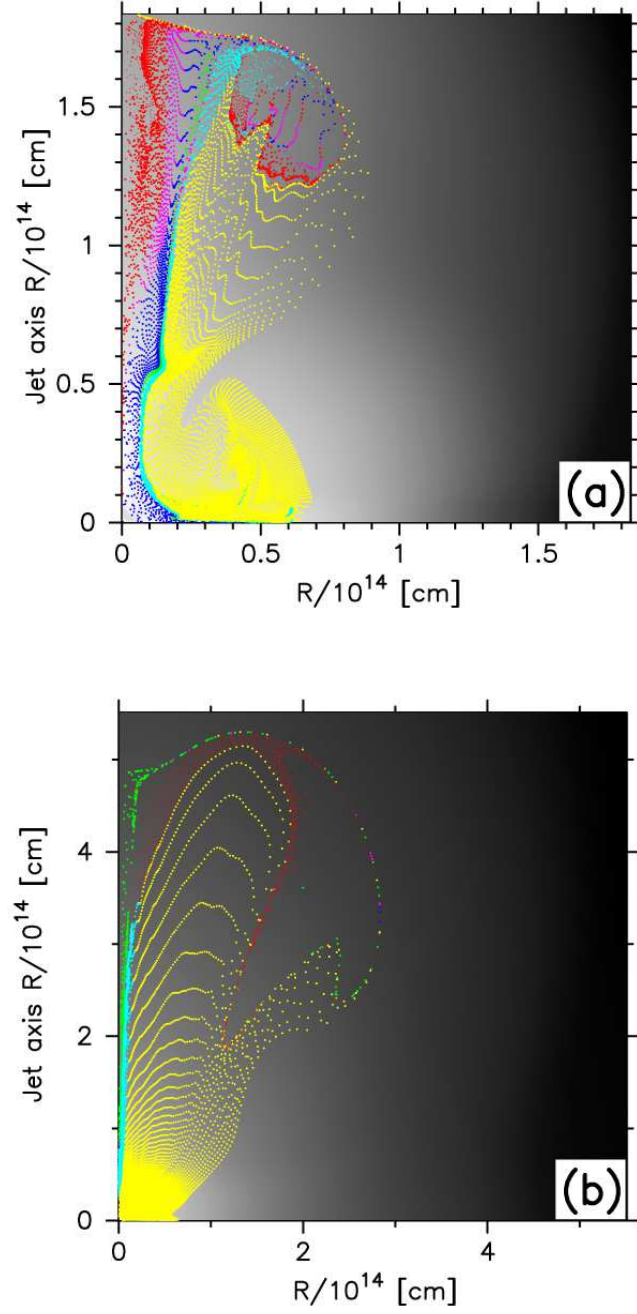


FIG. B4.— Density structure (*back ground gray scale*) and the position of the mass elements at $t = 10^5$ s for (a) model A and (b) model B. Color of the marks represents the abundance of the mass element (H: *yellow*, He: *cyan*, O+C: *green*, O+Mg: *blue*, Si: *magenta*, and Fe: *red*). Size of the marks represents the origin of the mass element (the jet: *dots*, and the shocked stellar mantle: *filled circles*).

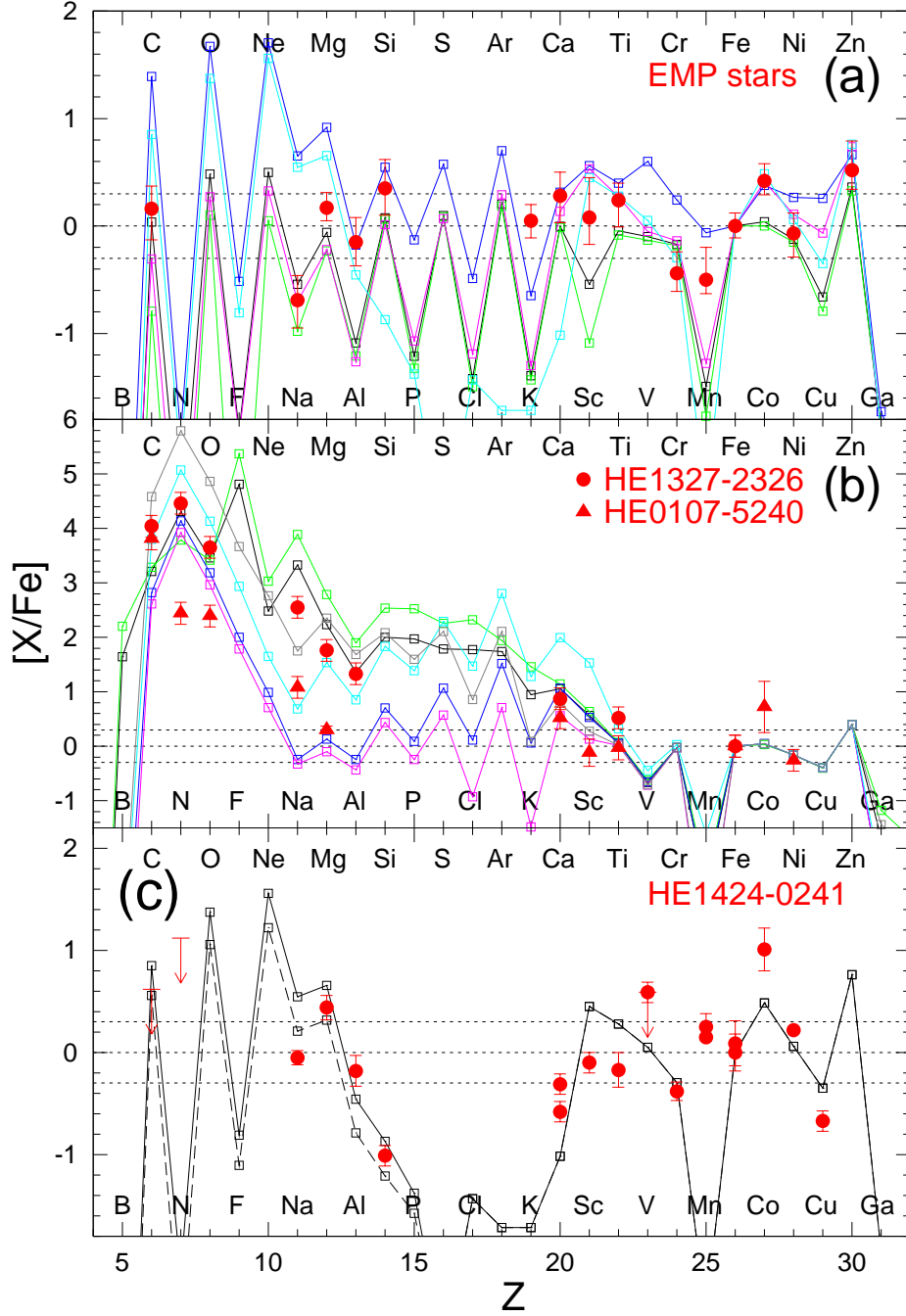


FIG. B5.— Comparison between the abundance patterns of the angle-integrated yield (black), the EMP and HMP stars (red filled marks), and the angle-delimited yields (colored) for (a) model A and (b) model B. The color of the lines represent the yields integrated over $0^\circ \leq \theta < 10^\circ$ (green), $10^\circ \leq \theta < 20^\circ$ (blue), $20^\circ \leq \theta < 30^\circ$ (magenta), $30^\circ \leq \theta < 40^\circ$ (cyan), and $40^\circ \leq \theta < 50^\circ$ (gray). (c) Comparison between the abundance pattern of HE 1424-0241 (red filled circles) and the angle-delimited yields of model A for $30^\circ \leq \theta < 40^\circ$ (solid line) and $30^\circ \leq \theta < 35^\circ$ (dashed line).

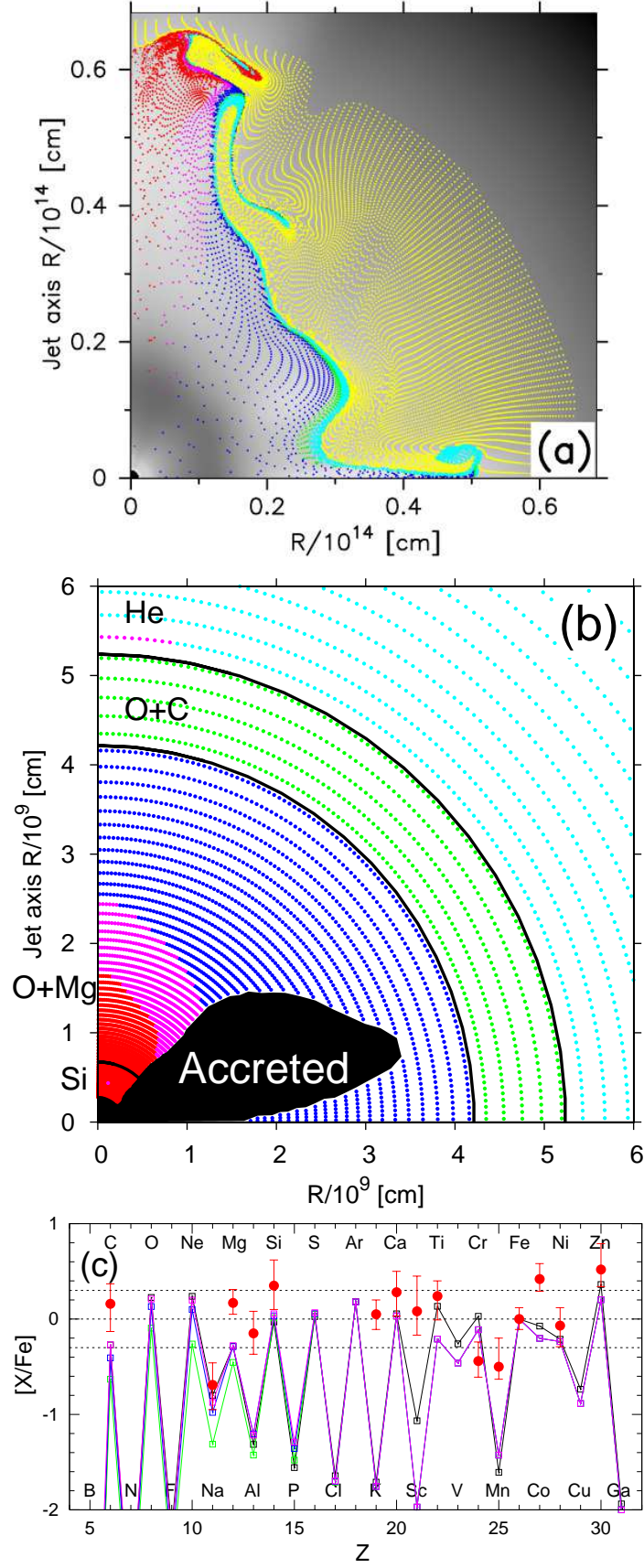


FIG. B6.— (a) Density structure (*back ground gray scale*) and the position of the mass elements at $t = 10^5$ s for model C. The color and size of the marks represent same as Figs. B4ab. (b) Initial locations of the mass elements which are finally accreted (*black*) and ejected (*colored points*) for model C. The color of the mass elements represents same as Figs. B4ab. (c) Comparison of the abundance patterns of model C (*black*), the EMP stars (*red circles*), and the mixing-fallback models with (1) $M_{\text{cut}}(\text{ini}) = 2.3M_{\odot}$, $M_{\text{mix}}(\text{out}) = 12.2M_{\odot}$ and $f = 0.41$ (*green*), (2) $M_{\text{cut}}(\text{ini}) = 2.3M_{\odot}$, $M_{\text{mix}}(\text{out}) = 10.3M_{\odot}$ and $f = 0.27$ (*blue*), and (3) $M_{\text{cut}}(\text{ini}) = 2.3M_{\odot}$, $M_{\text{mix}}(\text{out}) = 10.8M_{\odot}$ and $f = 0.19$ (*magenta*).

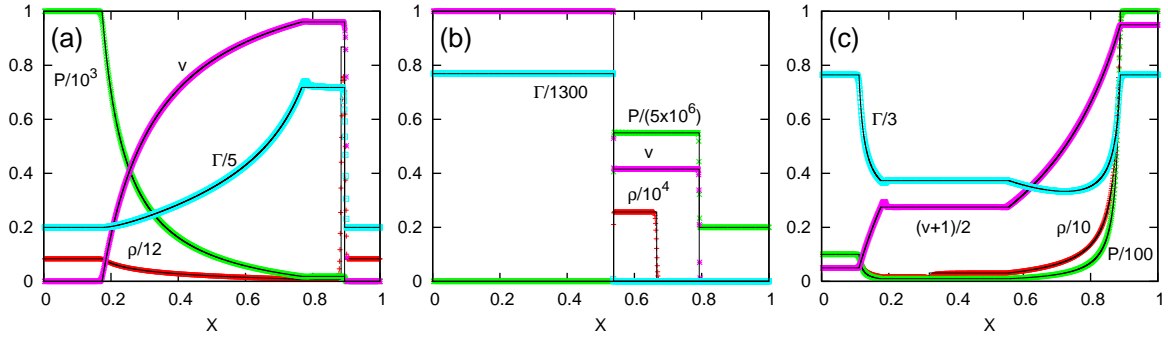


FIG. B7.— Comparison between the analytical solution of the Riemann problems (*black solid line*) and the results of the special relativistic hydrodynamics calculations (density: *red*, pressure: *green*, velocity: *magenta*, Lorentz factor: *cyan*).

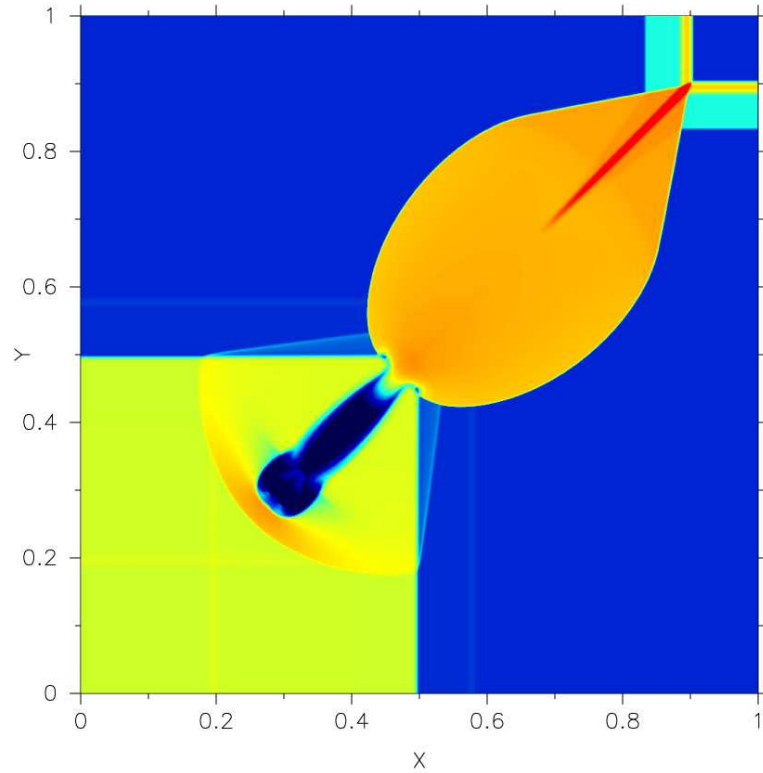


FIG. B8.— Two-dimensional shock tube problem at $t = 0.4$ with $10^3 \times 10^3$ square uniform meshes. Color contours of the logarithm of the rest mass density are plotted.

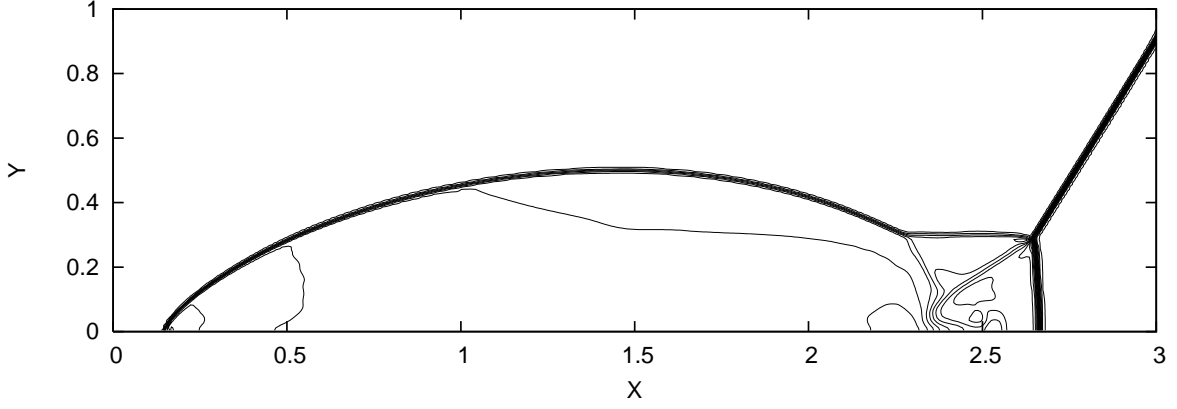


FIG. B9.— Double-Mach reflection problem at $t = 4.0$ with 512×128 uniform square meshes. Thirty equally-spaced contours of the logarithm of the rest mass density are plotted.

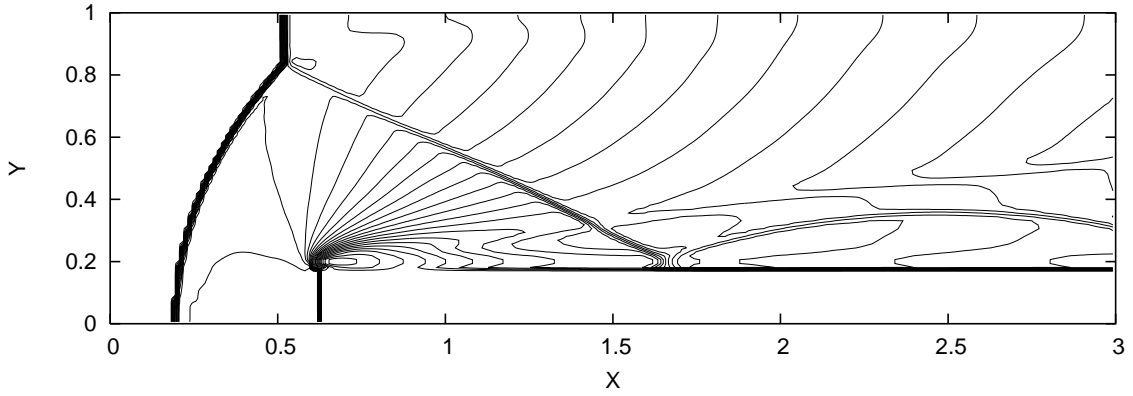


FIG. B10.— Emery step problem at $t = 4.0$ with 240×80 uniform square meshes. Thirty equally-spaced contours of the logarithm of the rest mass density are plotted.

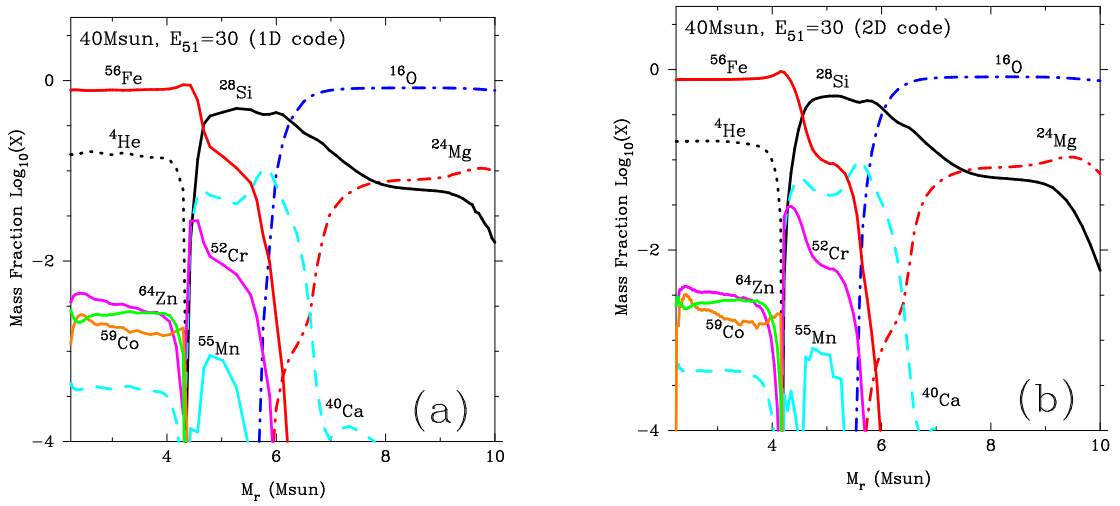


FIG. B11.— Abundance distributions after the non-relativistic spherical explosion of a $40M_{\odot}$ star with 3×10^{52} ergs. The post-processing calculations are performed with the thermodynamic histories obtained by (a) the one-dimensional spherical hydrodynamics code and (b) the two-dimensional special relativistic hydrodynamical code.